Elucidating Supercrystal Mechanics and Nanoparticle Size and Shape Effects Under High Pressure

Claire Hotton,[1o] Daniel García-Lojo,[2o] Evgeny Modin,[3o] Rahul Nag,[1] Sergio Gómez-Graña,[2] Jules Marcone,[1] Jaime Gabriel Trazo,[1] Jennifer Bodin,[1] Claire Goldmann,[1] Thomas Bizien,[4] Isabel Pastoriza-Santos,[2] Brigitte Pansu,[1*] Jorge Pérez-Juste,[2*] Victor Balédent,[1*] Cyrille Hamon[1*]

[1] Laboratoire de Physique des Solides, Université Paris-Saclay, CNRS, Orsay 91405, France.

[2] CINBIO, Universidade de Vigo, Departamento de Química Física, Campus Universitario As Lagoas, Marcosende, Vigo 36310, Spain.

[3] Electron Microscopy Laboratory CIC NanoGUNE BRTA Tolosa Hiribidea, 76, Donostia-San Sebastian 20019, Spain.

[4] SWING beamline, SOLEIL Synchrotron Gif-sur-Yvette 91190, France.

Keywords: Small angle X-ray scattering; high pressure; diamond anvil cell; FIB-SEM tomography; plasmonic nanoparticles

[o]: These authors contributed equally to this work (CH, DGL, EM)

E-mail: brigitte.pansu@universite-paris-saclay.fr; juste@uvigo.es; victor.baledent@universite-paris-saclay.fr; cyrille.hamon@universite-paris-saclay.fr

Abstract

Supercrystals, extended lattices of closely packed nanoparticles (NPs), present exciting possibilities for various applications. Under high pressures, typically in the gigapascal (GPa) range, supercrystals undergo significant structural changes, including adjustable inter-particle distances, phase transformations, and the formation of new nanostructures through coalescence. While prior research has focused on ligand engineering's impact on supercrystal mechanical response, the influence of NP shape remains unexplored, especially for NPs larger than 10 nm coated with hydrosoluble ligands. This study examines the effects of NP shape on the mechanical properties of supercrystals using high-pressure small-angle X-ray scattering (HP-SAXS) and focused ion beam-scanning electron microscopy (FIB-SEM) tomography. Notably, supercrystals exhibit higher hardness levels compared to previously reported values for gold supercrystals, attributed to the use of larger nanoparticles. Spherical and tetrahedral NPs rearrange before collapsing under pressure, whereas rods and octahedra coalesce without prior structural rearrangement, likely due to their higher packing fraction. Additionally, anisotropic deformation of NP lattices and sintering does not always correlate with deviatoric stresses. These findings refine the understanding of complex processes governing supercrystal structure under high pressure, opening new avenues for NP engineering and advancing plasmonic applications under extreme conditions.

Introduction

Colloidal self-assembly enables the spontaneous organization of nanoparticles (NPs) into well-defined and technologically relevant structures.[1] Extended lattices of close-packed nanoparticles, known as supercrystals, are emerging as a new class of matter, offering unique properties compared to bulk materials or individual building blocks.[1b] These supercrystals promise across various fields, including photonics and electronics to catalysis and sensing.[2] Since the precise positioning of NPs influences the collective properties of the material, one intriguing avenue is the *in situ* manipulation of the structure of the supercrystal. Among external stimuli, high pressures in the range of a few gigapascals (GPa) can induce profound structural modification such as tunable inter-particle distance, phase transformation and the formation of new nanostructures through pressure-induced coalescence.[3] While the effects of pressure on individual nanoparticles and bulk materials have been extensively studied,[3-4] our understanding of its impact on supercrystals is still in its nascent stages.

Since 2010, the scientific community has been exploring the mechanical properties of supercrystals and leveraging pressure-induced structural transformations. Various supercrystal compositions have been investigated such as Au,[5] PbS,[6] Co,[7] Pt,[8] Ag,[9] CdSe,[10] $CsPbBr_3$[11] and Fe_3O_4.[12] In general, supercrystals exhibit softness similar to hard polymer materials,[6a] primarily due to the ligands occupying the spaces between nanoparticles. The mechanical properties of supercrystals can be tailored by adjusting factors such as the length of the ligand,[13] the grafting density of the ligand on the NPs surface,[14] and through ligand cross-linking.[15] These properties have been determined through techniques such as indentation (uniaxial compression) or diamond anvil cell (DAC, hydrostatic compression). In a typical experiment involving supercrystals compressed in DAC, increasing pressure induces a reversible compression of the soft matrix up to a certain limit, beyond which the NPs coalesce into another structure. For instance, the oriented attachment of spherical NPs has led to the formation of nanosheets, nanowires, and heterostructures.[16] This structural transition and oriented attachment are often associated with the application of non-uniform deviatoric stress. While the majority of studies have concentrated on ligand engineering, only a few have explored the impact of NP shape to tailor the mechanical properties of supercrystals.[17] However, these works primarily concentrated on phase transformations at the nanoparticle level rather than at the supercrystal level. Although some works have studied the uniaxial compression of supercrystals built with hydrophilic ligands,[18] the majority of previous research has focused on supercrystals formed by small NPs (with sizes below 10 nm) coated

with hydrophobic ligands such as polystyrene, oleic acid, oleyamine, or alkanethiols.[3] There is a notable absence of similar investigations regarding larger NPs, non-spherical in shape, and coated with hydrophilic ligands.

The building blocks of supercrystals can be prepared using various methods. Among these, seed-mediated growth of metallic NPs stands out as a versatile approach for producing a diverse library of NP shapes, sizes, and compositions.[19] One of the most commonly used ligands employed in the seeded growth method is cetyltrimethylammonium chloride/bromide (CTAC/B), which forms a bilayer on the surface of nanoparticles, providing colloidal stability in water through steric and electrostatic repulsion.[20] Supercrystals have been obtained by evaporation-induced self-assembly (EISA)[21] with various NP shapes such as plates,[22] octahedra,[23] nanorods,[24] bipyramids,[25] or cubes.[26] Surprisingly, the mechanical properties of such materials have not yet been investigated, presumably due to the difficulties of manipulating the assemblies without damaging their structural integrity.

In this study, the mechanical properties of supercrystals are systematically tuned by varying the shape and size of the constituting metallic NPs. These supercrystals were examined in situ using high-pressure small-angle X-ray scattering (HP-SAXS) within a DAC and *ex-situ*, once returned to ambient pressure, by focused ion beam-scanning electron microscopy (FIB-SEM) tomography. In the first set of experiments, we conducted studies on supercrystals containing spherical NPs with diameters ranging from 37 to 58 nm. In a second set of experiments, we studied the mechanical properties of supercrystals composed of facetted and anisotropic NPs (octahedra, rods, and tetrahedra). We took advantage of the high ordering of the supercrystals to conduct a comprehensive analysis of their mechanical properties. In addition to determining the bulk modulus, we introduced new metrics to characterize pressure-induced structural transformations in the supercrystals. These metrics include the pressure threshold at which the lattice symmetry changes and the pressure at which nanoparticle collapse begins. Overall, this work expands our understanding of supercrystals under extreme conditions and is relevant for designing supercrystals with new lattice parameters, symmetry, and controlled disorder that are difficult to achieve through alternative methods.

Results and discussion

Formation of the supercrystals and description of the high-pressure setup.

A variety of metallic NPs were prepared by following previously reported seeded growth methodologies in water,[19] ensuring uniformity in both size and shape (see Table S1). Specifically, we prepared three batches of gold nanospheres (AuNS, ~37, 50 and 58 nm in diameter), two batches of gold octahedra (AuOh, 65 and 86 nm in edge length), one batch of gold tetrahedra (AuTh, 52 nm in edge length) and one batch of Au@Ag pentagonal nanorods (Au@AgNR, 217 nm in length and 31 nm in width). The comprehensive optical and structural analysis of these NPs was carried out through absorption spectroscopy, transmission electron microscopy (TEM), and SAXS (**Figures S1–S7** in the Supporting Information). All NPs present the same capping ligand, CTAC, and their assembly was triggered using a consistent CTAC concentration to mitigate ligand effects across samples and facilitate the comparative analysis (see details in the experimental section). For clarity, the NPs are denoted by their abbreviated names followed by their dimensions as a suffix (e.g. $AuNS_{58}$ for the gold nanospheres of 58 nm in diameter).

As illustrated in **Figure 1**, the formation of supercrystals was accomplished through two methods: microfluidic pervaporation (Pvap) and direct evaporation of a sessile drop (Evap). The Pvap method induces the NP self-assembly within microfluidic channels through slow solvent pervaporation via thin PDMS films.[27] After complete solvent evaporation, the resulting supercrystal conformed to the dimensions of the channels, measuring 300 μm in width, 25 μm in height, and spanning a few millimeters in length. The other approach, Evap, involved evaporating a sessile drop onto a Teflon substrate covered with a fluorinated oil layer.[28] This process led to a centralized deposition pattern, effectively minimizing the coffee ring effect by preventing contact line pinning. When comparing the extension of supercrystals obtained through both approaches, it becomes evident that the pervaporation technique leads to larger domains, in good agreement with our previous work (**Figure S8**).[29]

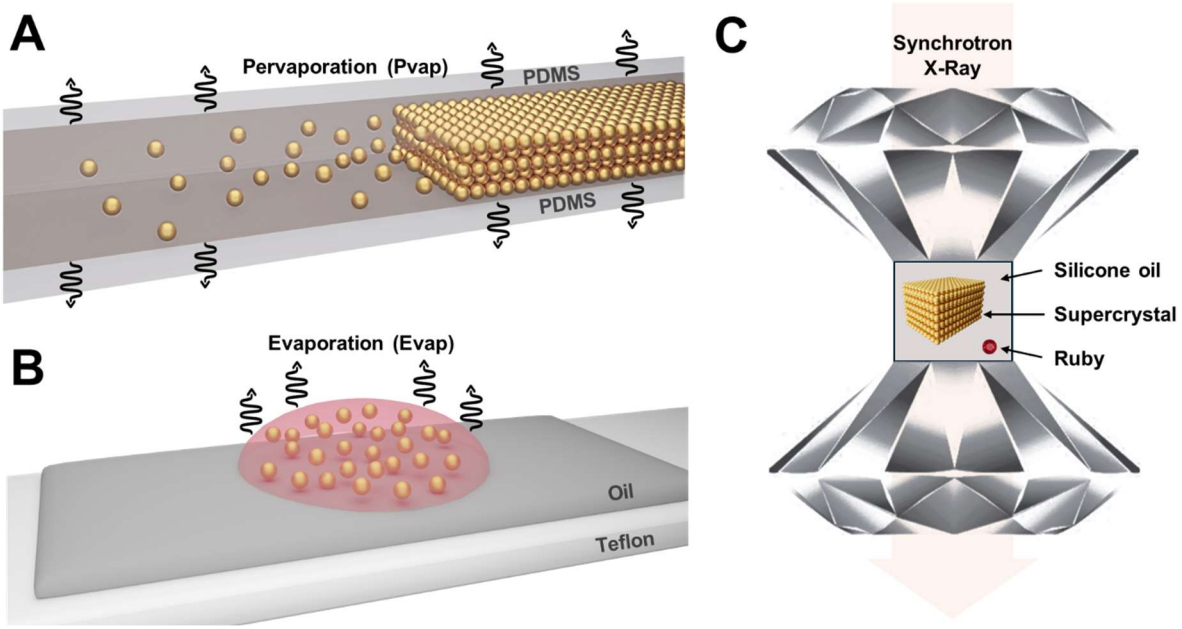

Figure 1. **Schematics of the two employed EISA methodologies to obtain supercrystals and the diamond anvil cell (DAC)**. A) Scheme of the Pvap process based on the pervaporation of colloidal NPs inside a microfluidic channel. B) Scheme of the Evap process based on the direct evaporation of a sessile drop over a fluorinated oil layer. C) Schematic representation of the experimental setup for HP-SAXS.

The large size of the supercrystal facilitated manipulation and loading into the DAC for the analysis of their mechanical properties under high pressure. Silicone oil was utilized as the pressure-transmitting medium due to its widespread use in the field, ensuring hydrostatic pressure and uniform compression up to 10 GPa.[30] Beyond this threshold, small deviatoric stress induces increased pressure along the compression axis. HP-SAXS experiments were conducted at a synchrotron source to generate sufficiently high X-ray energies capable of penetrating the DAC and enabling the measurement of the large lattice parameters within the supercrystals. Pressure was monitored *in situ* before and after each measurement using the standard pressure-dependent ruby fluorescence technique.[31] Diffractograms are derived by integrating 2D SAXS images and result from the interplay of the structure factor and form factor. The structure factor comprises information regarding the arrangement of nanoparticles, whereas the form factor encodes the scattering resulting from the size and shape of the nanoparticles. Previous studies focused on the evolution of the structure factor with the pressure, presumably because the small size of the NPs (typically below 10 nm) or limited q-range precluded monitoring the changes of the form factor, entangled and impossible to extract from the signal dominated by the structure factor. In this work, diffractograms are analyzed not only by the evolution of the structure but also by analyzing changes in the NP morphologies. At ambient pressure, supercrystals diffractograms are characterized by Bragg peaks at low q

and oscillations at higher q values, associated with structure factor and form factor respectively. For each supercrystal, we provide the evolution of the V/V_0 ratio with pressure for the different supercrystals, where V is the volume per particle and V_0 is its limit at ambient pressure. Note that V, and by extension V/V_0, do not accurately represent the actual volume when there is a significant change in the lattice parameter ratios or angles of the unit cell. This is why the increase in V under pressure is a signature of a structural transition, and the V/V_0 ratio loses its physical meaning above a certain pressure threshold. We also present the evolution of the form factor amplitude of the NPs on the same graph, which decreases with pressure as a result of the increase in polydispersity after the collapse of NPs. This representation serves to differentiate between two threshold pressures: one at which the NPs rearrange and one at which NPs collapse (hereafter referred to as P_t and P_c, respectively). P_t and P_c are estimated as shown in **Figure S9-S10**. The mechanical properties of the supercrystals are also discussed in terms of bulk modulus (the inverse volume compressibility, B_0) and are determined by fitting the V/V_0 evolution using the Rault model.[32] In the following, we describe the mechanics of AuNS supercrystals and, subsequently, of the various faceted NPs (**Table 1**). To complete this analysis, we conducted FIB-SEM tomography[33] on the supercrystals to examine the structure after the application of pressure and extraction from the DAC. For each sample, the pressure induced structural modification in the sample as shown by the non-reversibility in the *d* spacing upon releasing the pressure (**Figure S11-S12**).

Table 1. Mechanical properties of the supercrystals obtained with various Au NPs and via different self-assembly methods, as indicated. Pt is the pressure at which the symmetry of the supercrystals changes, Pc denotes the pressure at which NPs start collapsing, and B_0 is the bulk modulus. Pvap and Evap represent pervaporation in a microfluidic channel and EISA on a slippery substrate respectively.

NPs	Method	P_t (GPa)	P_c (GPa)	B_0 *(GPa)
$AuNS_{37}$	Pvap	5 ± 1	8.7 ± 0.1	3.1 ± 0.3
$AuNS_{37}$	Evap	2.5 ± 1	8.2 ± 1	3.2 ± 0.4
$AuNS_{50}$	Pvap	11.1 ± 1	15.3 ± 0.2	9.4 ± 0.4
$AuNS_{50}$	Evap	3.2 ± 1	7.0 ± 0.2	13.0 ± 0.7
$AuNS_{58}$	Pvap	5.2 ± 1	13.4 ± 0.9	34.8 ± 0.1
$AuOh_{64}$	Pvap	8.8 ± 1	8.3 ± 0.3	15.6 ± 0.2
$AuOh_{86}$	Pvap	1.2 ± 0.3	3.5 ± 0.4	9.7 ± 0.6
$AuTh_{50}$	Evap	5.0 ± 1.0	10.3 ± 0.5	17.8 ± 1.3
$Au@AgNR_{217\times31}$	Evap	9.4 ± 1.0	10.7 ± 0.4	16.5± 0.1

*Note that for non-spherical NPs, B_0 is estimated from the evolution of the position of one peak and considering isotropic deformation in volume.

Mechanical properties of AuNS supercrystals: size effects.

This section is devoted to study size effects on the mechanical properties of AuNS supercrystals, having a diameter ranging from 37 to 58 nm. We begin with discussing size effects and then focus on the mechanical properties of $AuNS_{58}$ supercrystal. AuNS are initially arranged in face-centered cubic (FCC) structures as indexed on the 2D SAXS images and diffractograms (**Figure 2A-C** and **Figure S13** on the ESI**)**. In all cases, the SAXS profiles show minimal evolution below 10 GPa, after which a dramatic transformation is observed in terms of peak position and number of peaks. Careful analysis of the V/V_0 ratio of the supercrystal reveals lattice compression at the initial pressure steps, followed by a plateau and subsequent lattice expansion (**Figure 2D,** and **Figure S11** on the ESI).

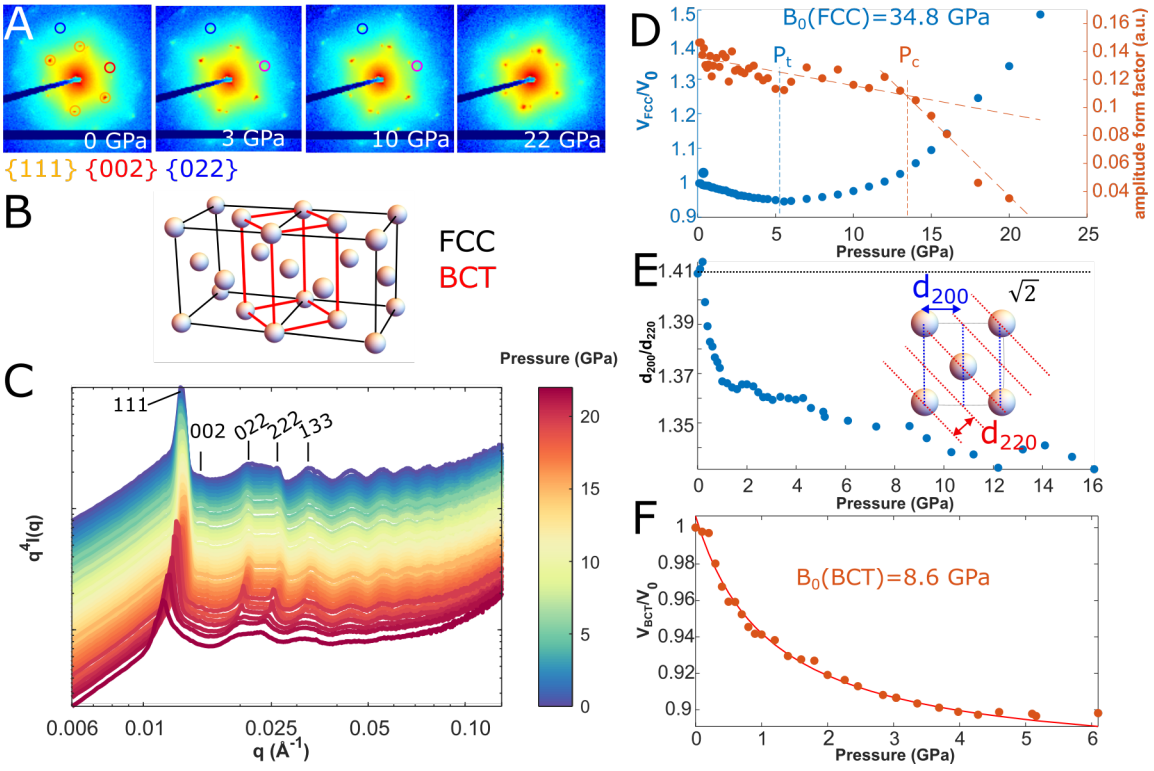

Figure 2. Structural evolution of $AuNS_{58}$ supercrystal obtained by pervaporation method during compression. A) HP-SAXS 2D images collected at varied pressures during compression for supercrystal composed of $AuNS_{58}$. B) Relation between FCC and BCT cells is seen through Bain's model.[34] C) HP-SAXS integrated diffractogram collected at varied pressures during compression for $AuNS_{58}$ supercrystal. The vertical lines indicate the expected positions of some Bragg peaks of an FCC lattice. D-F) Corresponding graphs showing the variation of some structural parameters upon increasing pressure. Variation of the ratio V/V_0 (blue points) (D), where V is the volume per particle and V_0 its limit at ambient pressure. We also present the progression of the amplitude of the form factor of the nanoparticles, illustrated

as orange points. The orange and blue vertical lines indicate P_t and P_c respectively. Variation of the ratio d_{200}/d_{220} (E) In the inset, d_{200} and d_{220} are defined along the {100} plane of the FCC unit cell. The variation of the ratio V/V_0 (F), was determined from d_{200} and d_{220}, assuming that the supercrystal deforms as a BCT lattice.

Initially, an abrupt decrease between ambient pressure and the first pressure steps was sometimes observed and can be attributed to the loss of solvent or void from the inter-particle gaps (**Figure S13C**).[3] After this initial volume change, the gradual decrease in V/V_0 can be attributed to lattice compression. As a result, the bulk modulus of the $AuNS_{37}$, $AuNS_{50}$ and $AuNS_{58}$ supercrystals was determined to be 3.1 GPa, 9.4 GPa, and 34.8 GPa, respectively. Note that the bulk modulus of supercrystals prepared by the two methods are consistent with each other (**Table 1**). While the mechanical properties of supercrystals of $AuNS_{37}$ and $AuNS_{50}$ are comparable to previous studies on supercrystals composed of smaller NPs coated with hydrophobic ligands,[6b, 35] the $AuNS_{58}$ supercrystal are significantly higher. These results show an increase in the stiffness of the supercrystals with the size of the NPs, a trend that is anticipated to further increase towards the bulk modulus of bulk gold (167 GPa).[36] This trend can also be understood by considering the gold volume fraction in the supercrystals, which is 45%, 55%, and 70% for $AuNS_{37}$, $AuNS_{50}$, and $AuNS_{58}$, respectively. In other words, there is more gold in the supercrystal as the size of the NPs increases while the ligand length remains constant. As a result, the bulk modulus of the supercrystal is expected to increase with the NP size toward the limit of 74% for the packing of perfect hard spheres.

After an initial decrease in the V/V_0 ratio as a function of pressure, all samples show a minimum that is generally attributed to the onset of particle collapse.[5, 16a] Note that if the NPs were indeed collapsing, the form factor (visible at high q values) would also change. In **Figure 2D**, it is evident that the pressure at which nanoparticles change in morphologies occurs at pressure values above the V/V_0 minimum. This discrepancy can be explained by the rearrangement of the NP lattice preceding the collapse of the NPs. While a clear identification of intermediary structures is challenging from the SAXS patterns, we were able to follow the evolution of some well-individualized peaks under pressure because the crystals made with $AuNS_{58}$ were of very good quality. Specifically, two spots q_{200} and q_{220}, corresponding respectively to the {200} and {220} plane families were followed. For an FCC lattice, the ratio of the distance between the planes (d_{200} and d_{220}) *is* $\frac{d200}{d220} = \sqrt{2}$. While this is the case at ambient pressure (**Figure 2E**), this ratio decreases significantly as soon as the pressure increases, revealing a continuous shift from an FCC to a BCT (body-centered tetragonal lattice, **Figure 2B**). The volume per particle in the BCT phase is $V = d_{200} \times d_{220}^2$. In line with this, we estimated

the bulk modulus of the BCT phase (8.6 GPa, **Figure 2F**), which is significantly lower than the bulk modulus value determined for the FCC structure (i.e. 34 GPa, **Figure 2D**). This experimental result indicates that the system does not respond homogeneously under hydrostatic pressure, suggesting the presence of areas more prone to deformation than others. One could argue that certain directions in the FCC lattice are more susceptible to deformation due to the non-homogeneous distribution of ligands. However, such a scenario would preserve the cubic symmetry, which is not consistent with our observations. We attribute this behavior to the presence of defects that break the symmetry of the system. While anisotropic deformation of the FCC lattice was previously suggested under uniaxial compression,[37] here we demonstrate that it can also occur under hydrostatic compression. In addition to showing unexpected mechanical properties, this analysis demonstrates that assuming uniform deformation of the supercrystal under pressure is a strong approximation and suggests that defects could drive the structural transition detected at pressure below 10 GPa. However, monitoring the displacement of individual Bragg spots on 2D SAXS images is challenging and necessitates highly oriented single-domain supercrystal. In this work, this analysis could only be conducted for the $AuNS_{58}$.

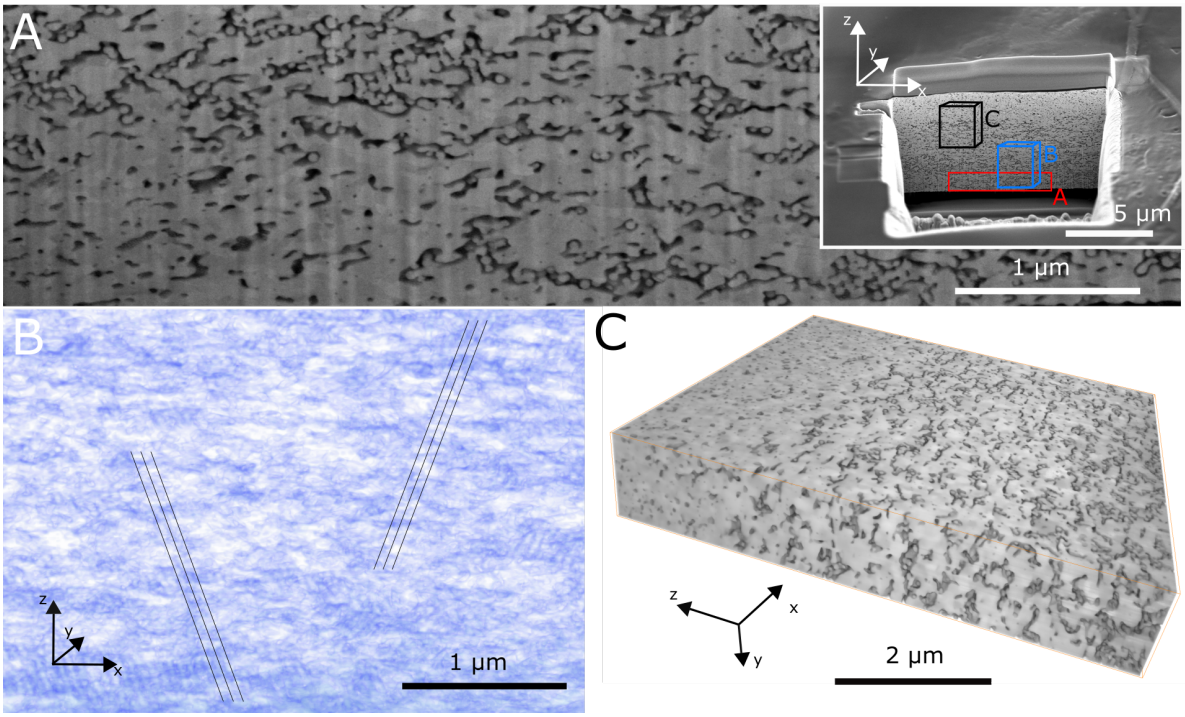

Figure 3. SEM characterization of the $AuNS_{58}$ supercrystal obtained employing the pervaporation methodology after returning to ambient pressure. A) SEM micrograph showing the cross-section of the nanosphere lattice. Inset is a view of a larger section of the supercrystal, onto which the images in A-C were taken. B-C) Three-dimensional

reconstructions of a portion of the supercrystal (inset in A), viewed along different orientations. In these images, NPs appear in light contrast, while voids are depicted in dark contrast.

After returning the $AuNS_{58}$ supercrystal to ambient pressure, we conducted FIB-SEM tomography (**Figure 3**). Since the supercrystal's macroscopic shape is anisotropic due to the fabrication method in microchannels, we ensured that the orientation of the supercrystals for the SEM was the same as for the DAC analysis. In **Figure 3,** the Z-axis corresponds to the direction of the X-ray beam in HP-SAXS experiments as well as the vertical orientation of the supercrystal in the DAC. Overall, the supercrystals exhibit a high degree of disorder, characterized by a mixture of sintered, partially sintered, and isolated nanoparticles. Small ordered domains are surrounded by fully fused regions, which can account for the broadening of the Bragg peak observed in HP-SAXS with increasing pressure. Additionally, oriented attachment around the vertical direction was observed, corresponding to the direction of higher pressure above 10 GPa. While such anisotropic deformation was suggested in DACs,[3] it is confirmed here by FIB SEM tomography within the supercrystal. In **Figure 3B**, two different directions of oriented attachment can be seen, revealing the presence of a twin plane in the supercrystal. The angle between the two planes is 60° which is the one expected between {110} and {011} planes, suggesting preferred sintering along (110) direction, in agreement with the literature.[9] These types of defects are presumably at the origin of the anisotropic deformation observed at intermediate pressure in HP-SAXS.

Mechanical properties of faceted NP supercrystals.

We next turn our focus on supercrystals composed of facetted NPs. The structure of the supercrystals no longer follows an FCC arrangement and instead depends on the shape of the building blocks. Determining the bulk modulus in these cases would require analyzing more peaks because of the lower symmetry of the unit cells. Despite our efforts, we were unable to carry out this analysis. Instead, we approximated it by analyzing the variation of the first peak in the diffractograms and treating the structures as FCC lattices. Although this is a rough estimation, the bulk modulus values obtained are consistent with those of the AuNSs (see **Table 1**).

Octahedra supercrystals were initially arranged in supercrystals with monoclinic *C2/m* symmetry, as identified from SAXS analysis and in agreement with our previous work (**Figure 4A**).[29]

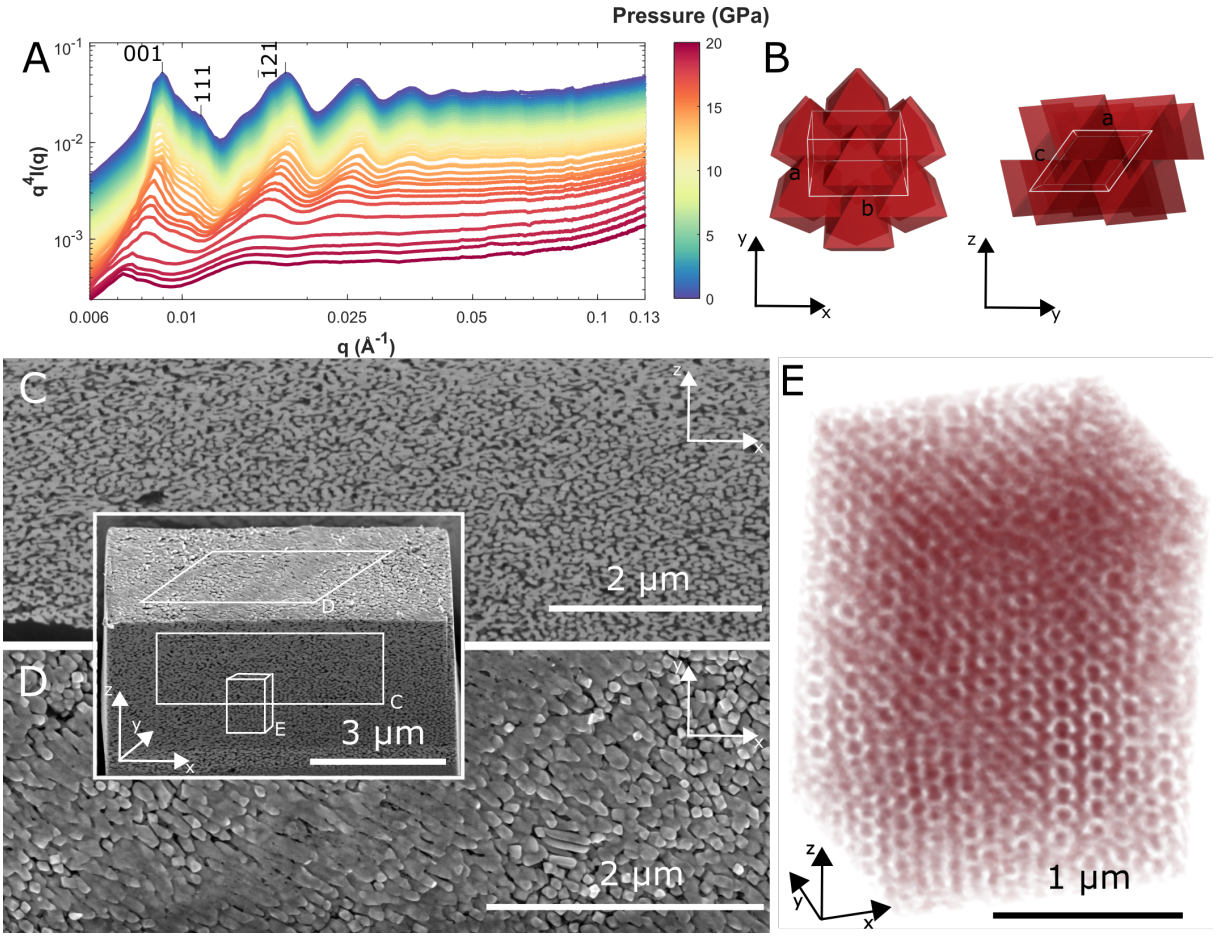

Figure 4. ***In situ*** **and** ***ex situ*** **characterization of the deformation of AuOh$_{86}$ supercrystal.** A) HP-SAXS integrated diffractogram collected at varied pressures during compression for AuOh$_{86}$ supercrystal. The vertical lines indicate the expected positions of some Bragg peaks of the monoclinic lattice. B) Schematic view of the unit cell before pressure-induced structural changes. C-E) Corresponding FIB-SEM tomography images after releasing the pressure. C-D) SEM micrographs showing the cross-section of the AuOh supercrystal viewed along different directions. Inset is a view of a larger section of the supercrystal, onto which the images in C-E were taken. NPs appear in light contrast, while voids are depicted in dark contrast. E) Three-dimensional reconstruction of a portion of the supercrystal where NPs are color-coded in red.

This structure corresponds to hexagonal monolayers stacked in an ABC fashion, with a relative offset of one layer to the next of 1/3 along the *c* monoclinic lattice direction (**Figure 4B**). Initially, we hypothesized that both AuOh supercrystals (AuOh$_{64}$ and AuOh$_{86}$) might recrystallize upon increasing the pressure, considering that octahedra are not arranged in the most compact structure (that is the Minkowski lattice[38]). However, we did not observe any significant change in lattice symmetry as the relative Bragg peak was shifted uniformly with the pressure. This suggests that the AuOh supercrystals do not rearrange significantly before collapsing. Instead, we observed that the deviation between the two threshold pressures (P_t and P_c) merges for AuOh$_{64}$ and AuOh$_{86}$, a feature markedly different compared to the nanospheres supercrystals (**Table 1**). This result can be understood by the higher packing fraction of

octahedra supercrystals (i.e. ≈ 89%) compared to nanosphere supercrystals (i.e. ≈ 74%), and increased Van der Waals interaction between NPs facets. Moreover, HP-SAXS analysis shows that NP collapse for the $AuOh_{86}$ occurs under hydrostatic pressure from 3.5 GPa. In the monoclinic lattice, there are several directions in which the octahedra are in contact: *a*, *(a+b)/2*, *(a-b)/2* and *c* (**Figure 4B**). Despite the original high symmetry of the lattice, the FIB-SEM tomography analysis revealed an oriented attachment between the octahedra with the pressure (**Figure 4C-E**, and **Figure S15-S16** on the ESI). HP-SAXS analysis shows that the supercrystal was oriented within the DAC along the (110) monoclinic lattice direction, with the *a.b* planes of the AuOh monolayers oriented perpendicular to the direction of maximum pressure (**Figure 4A**). Together, the results suggest the preferential sintering of the octahedra along the (001) monoclinic lattice direction. Although electronic microscopy images show some local ordering, the diffractogram after the release of the pressure did not evidence the formation of long-range structures (**Figure S12F-G** on the ESI). This supports the existence of a preferential deformation direction (presumably along (001) direction) in octahedra supercrystals but with attachment in other directions too, yielding to anisotropic nanostructures locally ordered across the supercrystal.

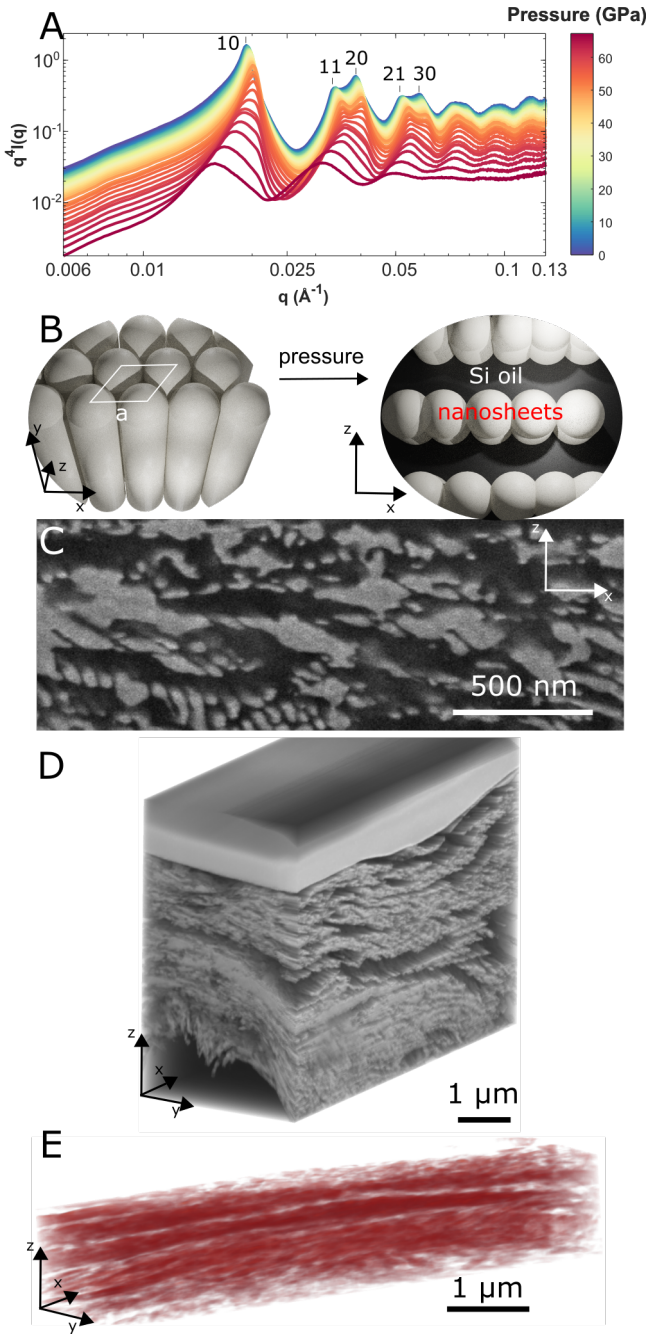

Figure 5. ***In situ*** **and** ***ex situ*** **characterization of the deformation of Au@AgNR$_{217\times31}$ supercrystals.** A) HP-SAXS integrated diffractogram collected at varied pressures during compression for Au@AgNR$_{217\times31}$ supercrystal. The vertical lines indicate the expected positions of some Bragg peaks of a hexagonal 2D lattice. B) Scheme of the unit cell and proposed deformation pathway for the lattice. C-E) Corresponding FIB-SEM tomography images after releasing the pressure. C) SEM micrograph showing the cross-section of the supercrystal. D-E) Three-dimensional reconstructions of a portion of the supercrystal. NPs in c-d appear in light contrast, while voids are depicted in dark contrast. In (E), NPs are color-coded in red.

Similar to the AuOh, Au@AgNR$_{189\times33}$ did not rearrange significantly before collapsing (**Table 1**). Although the bulk modulus of silver is lower than the one of gold (57 GPa[9] vs 167 GPa[36]),

the bulk modulus of the Au@AgNR$_{217\times31}$ supercrystal is in the same range as the gold supercrystals (**Table 1**). This is because the ligand coating of the NPs is consistent across all materials and drives the mechanical properties of the supercrystals. Au@AgNR$_{217\times31}$ formed hexagonal lattices consisting of monolayers without interlayer registry (**Figure 5A**).[39] The main axis of the rods was oriented perpendicular to the direction of increased pressure (**Figure 5B**). FIB-SEM tomography image analysis shows the formation of layered structures corresponding to alternating nanorods layers (in white) and organic matter (in black) (**Figure 5C-E**). Since the nanorods form a close-packed structure upon self-assembly, we determined that the silicon oil was intercalated in the supercrystal during the compression. Although the silicone oil is initially liquid, it turned solid after an irreversible phase transition during compression and remained solid after pressure release.[40] This resulted in the formation of the layered structures observed in FIB-SEM tomography. Layered composite materials of gold nanorods and silica have been obtained by a sol-gel process.[33a, 41] Our results show that other alternating inorganic/organic layered structures can be obtained under high pressure. The preferred direction of attachment is generally along the direction of increasing pressure. However, for the Au@AgNR$_{217\times31}$, the preferred attachment occurred perpendicular, that is along the (100) direction of the hexagonal layers. In this case, the organic spacer prevented the adjacent layers from sintering in the direction of pressure increase, leading to this unusual observation. Note that sintering was sometimes observed along the vertical direction where the NPs were not separated by the oil layer (**Figure S17** on the ESI). Together, these observations support the formation of 2D nanosheets from the nanorods layers through the intercalation of silicon oil into the supercrystal at high pressure.

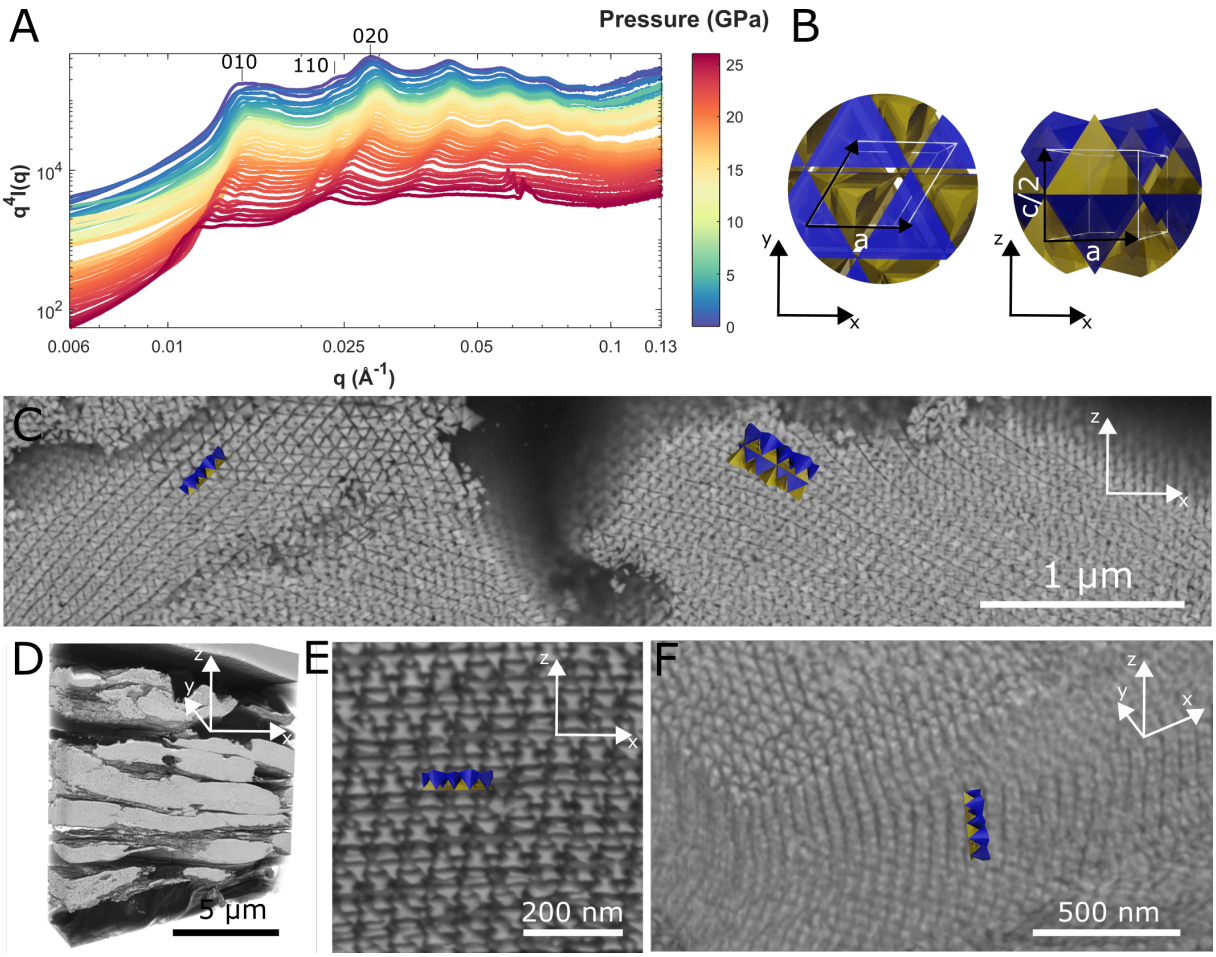

Figure 6. ***In situ*** **and** ***ex situ*** **characterization of the deformation of $AuTh_{50}$ supercrystals.** A) HP-SAXS integrated diffractogram collected at varied pressures during compression for $AuTh_{50}$ supercrystal. The vertical lines indicate the expected positions of some Bragg peaks of a *P3m1* trigonal lattice. B) Schematic view of the unit cell before pressure-induced structural changes. C-F) Corresponding FIB-SEM tomography images after releasing the pressure. C-D) SEM micrographs showing the cross-section of the AuTh supercrystal viewed along different directions. f) Three-dimensional reconstruction of a portion of the supercrystal. In these images, NPs appear in light contrast, while voids are depicted in dark contrast.

Gold tetrahedra are an emerging building blocks for self-assembly with many reported polymorphic structures.[42] This structural diversity can be understood by a competition between the structures that either maximize face-to-face contact or packing fraction. It was not possible to accurately determine lattice symmetry from the diffractograms in **Figure 6A** due to the broad Bragg peaks at ambient pressure. Nevertheless, they are consistent with the formation of trigonal *P3m1* lattices formed by intercalated hexagonal layers (**Figure 6B**).[42a] Differences in P_t and P_c indicate that lattice rearrangement occurs before NPs sintering (**Table 1**), whereas the precise determination of the phase transition could not be ruled out from HP-SAXS data. One possible pathway would be a sliding transformation between the blue and yellow tetrahedral layers to increase the packing fraction of the lattices, shifting the symmetry from

trigonal to centered rectangular.[42a, 42b] FIB-SEM image analysis revealed the formation of ordered structures (**Figure 6C-F**, and **Figure S18-19** on the ESI). Silicon oil intercalation in the $AuTh_{50}$ supercrystal was noted but to a lesser extent than in the case of $Au@AgNR_{217\times31}$ supercrystal (**Figure 6D**). Columnar structures of $AuTh_{50}$ were noted in different parts of the samples, showing sintering of the tetrahedra in the (100) and (010) directions of the trigonal lattice. Interestingly, the direction of preferential attachment is not the one where the tetrahedra share the most surface interaction (that is along (001) direction, **Figure 6B**). These findings provide support for a pressure-induced phase transition mechanism. The proposed mechanism involves the rotation and contraction of the blue and yellow lattices upon compression, ultimately resulting in the preferential sintering of the tetrahedra within the hexagonal layers rather than between the layers.

Conclusions

Our high-pressure diffraction experiment results on metallic NPs with different shapes and sizes have revealed several major points regarding their mechanical properties. The supercrystals exhibited a higher level of hardness than previously reported values for gold supercrystals, a feature that is attributed to the use of larger nanoparticle sizes. By separating the contributions related to the structure of the supercrystal and those related to the shape of the nanoparticles in HP-SAXS, we were able to highlight a three-step mechanism: a classical compression regime, a structural reorganization of the supercrystal, and, finally, a coalescence regime. This intermediate regime was expected and predicted in previous studies but not experimentally observed in HP-SAXS analysis due to the impossibility of disentangling the form factor from the structure factor. The rearrangement step was not observed in all cases. While spherical and tetrahedral NPs rearranged before collapsing, rods and octahedra coalesced without notable preceding structural rearrangement. This behavior can be attributed to their higher packing fraction than spherical and tetrahedral supercrystals. For the rods, the silicon oil intercalated within the layers under high pressure, yielding the formation of nanosheets orthogonally to the direction of increased pressure. Moreover, we have shown that anisotropic deformation of NPs lattice and sintering is not always correlated with deviatoric stresses. The insights gained from this study contribute to refine our understanding of the intricate processes governing supercrystal mechanics, opening avenues for NPs engineering and plasmonic applications under extreme conditions.

Supporting Information

Supporting Information is available from the Wiley Online Library or from the author.

Acknowledgments

The CNRS is acknowledged for funding and support. The authors thank Stéphan Rouzière for the use of the MORPHEUS platform. J.M. acknowledges financial support from the ANR NIMROD project (ANR-21-CE09-0019) for his PhD. R.N. acknowledges financial support from the ANR METATRAP project (ANR-22-CE09-0011). This work has benefited from an Investissements d'Avenir grant from Labex PALM (ANR-10-LABX-0039-PALM). The authors acknowledge SOLEIL for the provision of synchrotron radiation facilities (experiments 20221114, 20231786, SWING beamline). Authors acknowledge the support from MICIU/AEI/10.13039/501100011033 and ERDF/EU (Grant Number: PID2022-138724NB-I00) and the European Innovation Council (Horizon 2020 Project Number: 965018—BIOCELLPHE). Authors would like to acknowledge the use of scientific and technical services of Centro de Apoio Científico e Tecnolóxico á Investigación (CACTI-Universidade de Vigo). The present work has benefited from the electronic microscopy facility of Imagerie-Gif, (http://www.i2bc. parissaclay.fr), member of IBiSA (http://www.ibisa.net), supported by "France-BioImaging" (ANR10-INBS-04-01), and the Labex "Saclay Plant Science" (ANR-11-IDEX-0003-02). The authors thank Doru Constantin for constructive discussion of the manuscript.

References

[1] a) M. V. Kovalenko, L. Manna, A. Cabot, Z. Hens, D. V. Talapin, C. R. Kagan, V. I. Klimov, A. L. Rogach, P. Reiss, D. J. Milliron, P. Guyot-Sionnnest, G. Konstantatos, W. J. Parak, T. Hyeon, B. A. Korgel, C. B. Murray, W. Heiss, *ACS Nano* **2015**, 9, 1012; b) M. A. Boles, M. Engel, D. V. Talapin, *Chem. Rev.* **2016**, 116, 11220.

[2] a) J. Langer, D. Jimenez de Aberasturi, J. Aizpurua, R. A. Alvarez-Puebla, B. Auguie, J. J. Baumberg, G. C. Bazan, S. E. J. Bell, A. Boisen, A. G. Brolo, J. Choo, D. Cialla-May, V. Deckert, L. Fabris, K. Faulds, F. J. Garcia de Abajo, R. Goodacre, D. Graham, A. J. Haes, C. L. Haynes, C. Huck, T. Itoh, M. Kall, J. Kneipp, N. A. Kotov, H. Kuang, E. C. Le Ru, H. K. Lee, J. F. Li, X. Y. Ling, S. A. Maier, T. Mayerhofer, M. Moskovits, K. Murakoshi, J. M. Nam, S. Nie, Y. Ozaki, I. Pastoriza-Santos, J. Perez-Juste, J. Popp, A. Pucci, S. Reich, B. Ren, G. C. Schatz, T. Shegai, S. Schlucker, L. L. Tay, K. G. Thomas, Z. Q. Tian, R. P. Van Duyne, T. Vo-Dinh, Y. Wang, K. A. Willets, C. Xu, H. Xu, Y. Xu, Y. S. Yamamoto, B. Zhao, L. M. Liz-Marzan, *ACS Nano* **2020**, 14, 28; b) D. Garcia-Lojo, S. Nunez-Sanchez, S. Gomez-Grana, M. Grzelczak, I. Pastoriza-Santos, J. Perez-Juste, L. M. Liz-Marzan, *Acc. Chem. Res.* **2019**, 52,

1855; c) G. Baffou, R. Quidant, *Chem. Soc. Rev.* **2014**, 43, 3898; d) M.-P. Pileni, *J. Phys. Chem. C* **2021**, 125, 25936.

[3] F. Bai, K. Bian, X. Huang, Z. Wang, H. Fan, *Chem. Rev.* **2019**, 119, 7673.

[4] a) L. Meng, T. V. Vu, L. J. Criscenti, T. A. Ho, Y. Qin, H. Fan, *Chem. Rev.***2023**, 123, 10206; b) W. B. Holzapfel, *Rep. Prog. Phys. s* **1996**, 59, 29; c) S. H. Tolbert, A. P. Alivisatos, *Annu. Rev. Phys. Chem.* **1995**, 46, 595.

[5] H. Wu, F. Bai, Z. Sun, R. E. Haddad, D. M. Boye, Z. Wang, J. Y. Huang, H. Fan, *J. Am. Chem. Soc.* **2010**, 132, 12826.

[6] a) E. Tam, P. Podsiadlo, E. Shevchenko, D. F. Ogletree, M.-P. Delplancke-Ogletree, P. D. Ashby, *Nano Lett.* **2010**, 10, 2363; b) P. Podsiadlo, G. Krylova, B. Lee, K. Critchley, D. J. Gosztola, D. V. Talapin, P. D. Ashby, E. V. Shevchenko, *J. Am. Chem. Soc.* **2010**, 132, 8953.

[7] M. Gauvin, N. Yang, E. Barthel, I. Arfaoui, J. Yang, P. A. Albouy, M. P. Pileni, *J. Phys. Chem. C* **2015**, 119, 7483.

[8] J. Zhu, Z. Quan, C. Wang, X. Wen, Y. Jiang, J. Fang, Z. Wang, Y. Zhao, H. Xu, *Nanoscale* **2016**, 8, 5214; b) R. Li, J. Zhu, B. Ge, Z. Wang, *Chem. Mater.* **2023**, 35, 9412.

[9] B. Li, X. Wen, R. Li, Z. Wang, P. G. Clem, H. Fan, *Nat. Commun.* **2014**, 5, 4179.

[10] B. Li, K. Bian, X. Zhou, P. Lu, S. Liu, I. Brener, M. Sinclair, T. Luk, H. Schunk, L. Alarid, P. G. Clem, Z. Wang, H. Fan, *Sci. Adv.* **2017**, 3, e1602916.

[11] Y. Nagaoka, K. Hills-Kimball, R. Tan, R. Li, Z. Wang, O. Chen, *Adv. Mater.* **2017**, 29, 1606666.

[12] A. Dreyer, A. Feld, A. Kornowski, E. D. Yilmaz, H. Noei, A. Meyer, T. Krekeler, C. Jiao, A. Stierle, V. Abetz, H. Weller, G. A. Schneider, *Nat. Mater.* **2016**, 15, 522.

[13] M. Gauvin, Y. Wan, I. Arfaoui, M.-P. Pileni, *J. Phys. Chem. C* **2014**, 118, 5005.

[14] T. K. Patra, H. Chan, P. Podsiadlo, E. V. Shevchenko, S. K. R. S. Sankaranarayanan, B. Narayanan, *Nanoscale* **2019**, 11, 10655.

[15] A. Plunkett, M. Kampferbeck, B. Bor, U. Sazama, T. Krekeler, L. Bekaert, H. Noei, D. Giuntini, M. Fröba, A. Stierle, H. Weller, T. Vossmeyer, G. A. Schneider, B. Domènech, *ACS Nano* **2022**, 16, 11692.

[16] a) H. Wu, F. Bai, Z. Sun, R. E. Haddad, D. M. Boye, Z. Wang, H. Fan, *Angew. Chem. Int. Ed.* **2010**, 49, 8431; b) Z. Wang, C. Schliehe, T. Wang, Y. Nagaoka, Y. C. Cao, W. A. Bassett, H. Wu, H. Fan, H. Weller, *J. Am. Chem. Soc.* **2011**, 133, 14484; c) H. Zhu, Y. Nagaoka, K. Hills-Kimball, R. Tan, L. Yu, Y. Fang, K. Wang, R. Li, Z. Wang, O. Chen, *J. Am. Chem. Soc.* **2017**, 139, 8408.

[17] a) N. J. Lee, R. K. Kalia, A. Nakano, P. Vashishta, *Appl. Phys. Lett.* **2006**, 89; b) L. Meng, J. M. D. Lane, L. Baca, J. Tafoya, T. Ao, B. Stoltzfus, M. Knudson, D. Morgan, K. Austin, C. Park, P. Chow, Y. Xiao, R. Li, Y. Qin, H. Fan, *J. Am. Chem. Soc.* **2020**, 142, 6505; c) S.-w. Park, J.-t. Jang, J. Cheon, H.-H. Lee, D. R. Lee, Y. Lee, *J. Phys. Chem. C* **2008**, 112, 9627; d) T. Xiao, Y. Nagaoka, X. Wang, T. Jiang, D. LaMontagne, Q. Zhang, C. Cao, X. Diao, J. Qiu, Y. Lu, Z. Wang, Y. C. Cao, *Science* **2022**, 377, 870; e) S. Jiang, X. Chen, X. Huang, C. Li, Z. Wang, B. Zhao, L. Zhang, G. Zhou, J. Fang, *J. Am. Chem. Soc.* **2024**, 146, 8598.

[18] a) Y. Li, H. Jin, W. Zhou, Z. Wang, Z. Lin, C. A. Mirkin, H. D. Espinosa, *Sci. Adv.* **2023**, 9, eadj8103; b) S. Dhulipala, D. W. Yee, Z. Zhou, R. Sun, J. E. Andrade, R. J. Macfarlane, C. M. Portela, *Nano Lett.* **2023**, 23, 5155.

[19] Y. Xia, K. D. Gilroy, H. C. Peng, X. Xia, *Angew. Chem. Int. Ed.* **2017**, 56, 60.

[20] a) S. Gomez-Grana, F. Hubert, F. Testard, A. Guerrero-Martinez, I. Grillo, L. M. Liz-Marzan, O. Spalla, *Langmuir* **2012**, 28, 1453; b) C. J. Murphy, L. B. Thompson, A. M. Alkilany, P. N. Sisco, S. P. Boulos, S. T. Sivapalan, J. A. Yang, D. J. Chernak, J. Y. Huang, *J. Phys. Chem. Lett.* **2010**, 1, 2867.

[21] W. Han, Z. Lin, *Angew. Chem. Int. Ed.* **2012**, 51, 1534.

[22] J. Kim, X. Song, F. Ji, B. Luo, N. F. Ice, Q. Liu, Q. Zhang, Q. Chen, *Nano Lett.* **2017**, 17, 3270.

[23] J. Gong, R. S. Newman, M. Engel, M. Zhao, F. Bian, S. C. Glotzer, Z. Tang, *Nat. Commun.* **2017**, 8, 14038.

[24] J. Marcone, W. Chaabani, C. Goldmann, M. Imperor-Clerc, D. Constantin, C. Hamon, *Nano Lett.* **2023**, 23, 1337.

[25] J. Lyu, W. Chaabani, E. Modin, A. Chuvilin, T. Bizien, F. Smallenburg, M. Imperor-Clerc, D. Constantin, C. Hamon, *Adv. Mater.* **2022**, 34, e2200883.

[26] H. Chan, A. Demortiere, L. Vukovic, P. Kral, C. Petit, *ACS Nano* **2012**, 6, 4203.

[27] a) A. Merlin, J.-B. Salmon, J. Leng, *Soft Matter* **2012**, 8, 3526; b) P. Bacchin, J. Leng, J. B. Salmon, *Chem. Rev.* **2022**, 122, 6938.

[28] S. Yang, X. Dai, B. B. Stogin, T.-S. Wong, *Proc. Natl. Acad. Sci. U.S.A.* **2016**, 113, 268.

[29] D. García-Lojo, E. Modin, S. Gómez-Graña, M. Impéror-Clerc, A. Chuvilin, I. Pastoriza-Santos, J. Pérez-Juste, D. Constantin, C. Hamon, *Adv. Funct. Mater.* **2021**, 31, 2101869.

[30] N. Tateiwa, Y. Haga, *Rev. Sci. Instrum.* **2009**, 80.

[31] A. D. Chijioke, W. J. Nellis, A. Soldatov, I. F. Silvera, *J. Appl. Phys.* **2005**, 98.

[32] J. Rault, *Eur. Phys. J. E* **2014**, 37, 113.

[33] a) C. Hamon, M. N. Sanz-Ortiz, E. Modin, E. H. Hill, L. Scarabelli, A. Chuvilin, L. M. Liz-Marzan, *Nanoscale* **2016**, 8, 7914; b) F. Mura, F. Cognigni, M. Ferroni, V. Morandi, M. Rossi, *Materials* **2023**, 16, 5808; c) J. E. S. van der Hoeven, E. B. van der Wee, D. A. M. de Winter, M. Hermes, Y. Liu, J. Fokkema, M. Bransen, M. A. van Huis, H. C. Gerritsen, P. E. de Jongh, A. van Blaaderen, *Nanoscale* **2019**, 11, 5304.

[34] E. C. Bain, *Trans. Am. Inst. Miner. Metall. Eng.* **1924**, 70, 25.

[35] a) P. Podsiadlo, B. Lee, V. B. Prakapenka, G. V. Krylova, R. D. Schaller, A. Demortière, E. V. Shevchenko, *Nano Lett.* **2011**, 11, 579; b) H. Ibrahim, V. Balédent, M. Impéror-Clerc, B. Pansu, *RSC Adv.* **2022**, 12, 23675; c) V. Balédent, C. Goldmann, H. Ibrahim, B. Pansu, *Soft Matter* **2023**, 19, 3113.

[36] J. Boettger, K. G. Honnell, J. H. Peterson, C. Greeff, S. Crockett, *AIP Conf. Proc.* **2012**, 1426, 812.

[37] a) W. Li, H. Fan, J. Li, *Nano Letters* **2014**, 14, 4951; b) B. Li, K. Bian, J. M. D. Lane, K. M. Salerno, G. S. Grest, T. Ao, R. Hickman, J. Wise, Z. Wang, H. Fan, *Nat. Commun.* **2017**, 8, 14778.

[38] a) J. Henzie, M. Grünwald, A. Widmer-Cooper, P. L. Geissler, P. Yang, *Nat. Mater.* **2012**, 11, 131; b) S. Torquato, Y. Jiao, *Nature* **2009**, 460, 876.

[39] a) J. A. C. Veerman, D. Frenkel, *Phys. Rev. A* **1991**, 43, 4334; b) C. Hamon, M. Postic, E. Mazari, T. Bizien, C. Dupuis, P. Even-Hernandez, A. Jimenez, L. Courbin, C. Gosse, F. Artzner, V. Marchi-Artzner, *ACS Nano* **2012**, 6, 4137.

[40] B. Sundqvist, *Rev. Sci. Instrum.* **2005**, 76.

[41] G. Bodelon, V. Montes-Garcia, V. Lopez-Puente, E. H. Hill, C. Hamon, M. N. Sanz-Ortiz, S. Rodal-Cedeira, C. Costas, S. Celiksoy, I. Perez-Juste, L. Scarabelli, A. La Porta, J. Perez-Juste, I. Pastoriza-Santos, L. M. Liz-Marzan, *Nat. Mater.* **2016**, 15, 1203.

[42] a) Y. Wang, J. Chen, Y. Zhong, S. Jeong, R. Li, X. Ye, *J. Am. Chem. Soc.* **2022**, 144, 13538; b) Z. Cheng, M. R. Jones, *Nat. Commun.* **2022**, 13, 4207; c) S. Zhou, J. Li, J. Lu, H. Liu, J.-Y. Kim, A. Kim, L. Yao, C. Liu, C. Qian, Z. D. Hood, X. Lin, W. Chen, T. E. Gage, I. Arslan, A. Travesset, K. Sun, N. A. Kotov, Q. Chen, *Nature* **2022**, 612, 259.